

Dark matter, electroweak phase transition and gravitational wave in the type-II two-Higgs-doublet model with a singlet scalar field

Xiao-Fang Han¹, Lei Wang¹, Yang Zhang^{2,3}

¹ *Department of Physics, Yantai University, Yantai 264005, P. R. China*

² *School of Physics, Zhengzhou University, ZhengZhou 450001, P. R. China*

³ *ARC Centre of Excellence for Particle Physics at the Tera-scale,*

School of Physics and Astronomy, Monash University,

Melbourne, Victoria 3800, Australia

Abstract

In the framework of type-II two-Higgs-doublet model with a singlet scalar dark matter S , we study the dark matter observables, the electroweak phase transition, and the gravitational wave signals by such strongly first order phase transition after imposing the constraints of the LHC Higgs data. We take the heavy CP-even Higgs H as the only portal between the dark matter and SM sectors, and find the LHC Higgs data and dark matter observables require m_S and m_H to be larger than 130 GeV and 360 GeV for $m_A = 600$ GeV in the case of the 125 GeV Higgs with the SM-like coupling. Next, we carve out some parameter space where a strongly first order electroweak phase transition can be achieved, and find benchmark points for which the amplitudes of gravitational wave spectra reach the sensitivities of the future gravitational wave detectors.

I. INTRODUCTION

The weakly interacting massive particle is a primary candidate for dark matter (DM) in the present Universe. Many extensions of SM have been proposed to provide a candidate of DM, and one simple extension is to add a singlet scalar DM to the type-II two-Higgs-doublet model (2HDM) [1–3]. The type-II 2HDM (2HDMIID) contains two CP-even states, h and H , one neutral pseudoscalar A , two charged scalars H^\pm , and one CP-even singlet scalar S as the candidate of DM [4–14].

In the type-II 2HDM model, the Yukawa couplings of the down-type quark and lepton can be both enhanced by a factor of $\tan\beta$. Therefore, the flavor observables and the LHC searches for Higgs can impose strong constraints on type-II 2HDM model. In the 2HDMIID, the two CP-even states h and H may be portals between the DM and SM sectors, and there are plentiful parameter space satisfying the direct and indirect experimental constraints of DM. The scalar potential of 2HDMIID contains the original one of type-II 2HDM and one including DM. For appropriate Higgs mass spectrum and coupling constants, the type-II 2HDM can trigger a strong first-order electroweak phase transition (SFOEWPT) in the early universe [15–18], which is required by a successful explanation of the observed baryon asymmetry of the universe (BAU) [19] and can produce primordial gravitational wave (GW) signals [20].

In this paper, we first examine the parameter space of the 2HDMIID using the recent LHC Higgs data and DM observables. After imposing various theoretical and experimental constraints, we analyze whether a SFOEWPT is achievable in the 2HDMIID, and discuss the resultant GW signals and its detectability at the future GW detectors, such as LISA [21], Taiji [22], TianQin [23], Big Bang Observer (BBO) [24], DECi-hertz Interferometer GW Observatory (DECIGO) [24] and Ultimate- DECIGO [25].

Our work is organized as follows. In Sec. II we will give a brief introduction on the 2HDMIID. In Sec. III and Sec. IV, we show the allowed parameter space after imposing the limits of the LHC Higgs data and DM observables. In Sec. V, we examine the parameter space leading to a SFOEWPT and the corresponding GW signal. Finally, we give our conclusion in Sec. VI.

II. TYPE-II TWO-HIGGS-DOUBLET MODEL WITH A SCALAR DARK MATTER

The scalar potential of 2HDMIID is given as [26]

$$\begin{aligned}
\mathcal{V}_{tree} = & m_{11}^2(\Phi_1^\dagger\Phi_1) + m_{22}^2(\Phi_2^\dagger\Phi_2) - \left[m_{12}^2(\Phi_1^\dagger\Phi_2 + \text{h.c.}) \right] \\
& + \frac{\lambda_1}{2}(\Phi_1^\dagger\Phi_1)^2 + \frac{\lambda_2}{2}(\Phi_2^\dagger\Phi_2)^2 + \lambda_3(\Phi_1^\dagger\Phi_1)(\Phi_2^\dagger\Phi_2) + \lambda_4(\Phi_1^\dagger\Phi_2)(\Phi_2^\dagger\Phi_1) \\
& + \left[\frac{\lambda_5}{2}(\Phi_1^\dagger\Phi_2)^2 + \text{h.c.} \right] \\
& + \frac{1}{2}S^2(\kappa_1\Phi_1^\dagger\Phi_1 + \kappa_2\Phi_2^\dagger\Phi_2) + \frac{m_0^2}{2}S^2 + \frac{\lambda_S}{4!}S^4.
\end{aligned} \tag{1}$$

Here we discuss the CP-conserving model in which all λ_i , κ_i and m_{12}^2 are real. The S is a real singlet scalar field, and Φ_1 and Φ_2 are complex Higgs doublets with hypercharge $Y = 1$:

$$\Phi_1 = \begin{pmatrix} \phi_1^+ \\ \frac{1}{\sqrt{2}}(v_1 + \phi_1^0 + ia_1) \end{pmatrix}, \quad \Phi_2 = \begin{pmatrix} \phi_2^+ \\ \frac{1}{\sqrt{2}}(v_2 + \phi_2^0 + ia_2) \end{pmatrix}. \tag{2}$$

Where v_1 and v_2 are the electroweak vacuum expectation values (VEVs) with $v^2 = v_1^2 + v_2^2 = (246 \text{ GeV})^2$, and the ratio of the two VEVs is defined as $\tan \beta = v_2/v_1$. The linear and cubic terms of the S field are forbidden by a Z'_2 symmetry, under which $S \rightarrow -S$. The S is a possible DM candidate since it does not acquire a VEV. After spontaneous electroweak symmetry breaking, the remaining physical states are three neutral CP-even states h , H , and S , one neutral pseudoscalar A , and two charged scalars H^\pm .

We can obtain the DM mass and the cubic interactions with the neutral Higgses from Eq. (1),

$$\begin{aligned}
m_S^2 &= m_0^2 + \frac{1}{2}\kappa_1 v^2 \cos^2 \beta + \frac{1}{2}\kappa_2 v^2 \sin^2 \beta, \\
-\lambda_h v S^2 h/2 &\equiv -(\kappa_1 \sin \alpha \cos \beta + \kappa_2 \cos \alpha \sin \beta) v S^2 h/2, \\
-\lambda_H v S^2 H/2 &\equiv -(\kappa_1 \cos \alpha \cos \beta + \kappa_2 \sin \alpha \sin \beta) v S^2 H/2,
\end{aligned} \tag{3}$$

with α being the mixing angle of h and H .

The Yukawa interactions are written as

$$-\mathcal{L} = Y_{u2} \bar{Q}_L \tilde{\Phi}_2 u_R + Y_{d1} \bar{Q}_L \Phi_1 d_R + Y_{\ell 1} \bar{L}_L \Phi_1 e_R + \text{h.c.}, \tag{4}$$

where $Q_L^T = (u_L, d_L)$, $L_L^T = (\nu_L, l_L)$, $\tilde{\Phi}_{1,2} = i\tau_2 \Phi_{1,2}^*$, and Y_{u2} , Y_{d1} and $Y_{\ell 1}$ are 3×3 matrices in family space.

The Yukawa couplings of the neutral Higgs bosons normalized to the SM are given by

$$\begin{aligned}
y_h^{f_i} &= [\sin(\beta - \alpha) + \cos(\beta - \alpha)\kappa_f], \\
y_H^{f_i} &= [\cos(\beta - \alpha) - \sin(\beta - \alpha)\kappa_f], \\
y_A^{f_i} &= -i\kappa_f \text{ (for } u), \quad y_A^{f_i} = i\kappa_f \text{ (for } d, \ell), \\
&\text{with } \kappa_d = \kappa_\ell \equiv -\tan\beta, \quad \kappa_u \equiv 1/\tan\beta.
\end{aligned} \tag{5}$$

The charged Higgs has the following Yukawa interactions,

$$\mathcal{L}_Y = -\frac{\sqrt{2}}{v} H^+ \left\{ \bar{u}_i [\kappa_d (V_{CKM})_{ij} m_{dj} P_R - \kappa_u m_{ui} (V_{CKM})_{ij} P_L] d_j + \kappa_\ell \bar{\nu} m_\ell P_R \ell \right\} + h.c., \tag{6}$$

where $i, j = 1, 2, 3$.

The neutral Higgs boson couplings with the gauge bosons normalized to the SM are given by

$$y_h^V = \sin(\beta - \alpha), \quad y_H^V = \cos(\beta - \alpha), \tag{7}$$

where V denotes Z or W . In the type-II 2HDM, the 125 GeV Higgs is allowed to have the SM-like coupling and wrong sign Yukawa coupling,

$$\begin{aligned}
y_h^{f_i} \times y_h^V &> 0 \text{ for SM-like coupling,} \\
y_h^{f_i} \times y_h^V &< 0 \text{ for wrong sign Yukawa coupling.}
\end{aligned} \tag{8}$$

III. THE EXPERIMENTAL CONSTRAINTS OF THE HIGGS DATA AT THE LHC

A. Numerical calculations

We take the light CP-even Higgs boson h as the SM-like Higgs, $m_h = 125$ GeV. The measurement of the branching fraction of $b \rightarrow s\gamma$ gives the stringent constraints on the charged Higgs mass of the type-II 2HDM, $m_{H^\pm} > 570$ GeV [27]. If the 125 GeV Higgs boson is the portal between the DM and SM sectors, it is favored to have wrong sign Yukawa coupling which can realize the isospin-violating DM interactions with nucleons and relax the bounds of direct detection of DM. However, Ref. [17] shows the the wrong sign Yukawa coupling region of type-II 2HDM is strongly restricted by the requirement of SFOEWPT.

Therefore, in this paper we take the heavy CP-even Higgs H as the only portal between the DM and SM sectors, and focus on the case of the 125 GeV with the SM-like coupling. The S , T , and U oblique parameters give the stringent constraints on the mass spectrum of Higgses of type-II 2HDM [28–30]. One of m_A and m_H is around 600 GeV, and another is allowed to have a wide mass range including low mass [29, 30]. Therefore, we fix $m_A = 600$ GeV to make the portal H to have a wide mass range.

In our calculation, we consider the following observables and constraints:

- (1) Theoretical constraints. The scalar potential of the model contains one of the type-II 2HDM and one of the DM sector. The vacuum stability, perturbativity, and tree-level unitarity impose constraints on the relevant parameters, which are discussed in detail in Refs. [8, 9]. Here we employ the formulas in [8, 9] to implement the theoretical constraints. Compared to Refs. [8, 9], there are additional factors of $\frac{1}{2}$ in the κ_1 term and the κ_2 term of this paper. In addition, we require that the potential has a global minimum at the point of ($\langle h_1 \rangle = v_1$, $\langle h_2 \rangle = v_2$, $\langle S_1 \rangle = 0$).
- (2) The oblique parameters. The S , T , U parameters can impose stringent constraints on the mass spectrum of Higgses of 2HDM. We use 2HDMC [31] to calculate the S , T , U parameters. Taking the recent fit results of Ref. [32], we use the following values of S , T , U ,

$$S = 0.02 \pm 0.10, \quad T = 0.07 \pm 0.12, \quad U = 0.00 \pm 0.09. \quad (9)$$

The correlation coefficients are

$$\rho_{ST} = 0.89, \quad \rho_{SU} = -0.54, \quad \rho_{TU} = -0.83. \quad (10)$$

- (3) The flavor observables and R_b . We employ SuperIso-3.4 [33] to calculate $Br(B \rightarrow X_s \gamma)$, and Δm_{B_s} is calculated following the formulas in [34]. Besides, we include the constraints of bottom quarks produced in Z decays, R_b , which is calculated following the formulas in [35, 36].
- (4) The global fit to the 125 GeV Higgs signal data. The version 2.0 of Lilith [37] is used to perform the χ^2 calculation for the signal strengths of the 125 GeV Higgs combining the LHC run-I and run-II data (up to datasets of 36 fb^{-1}). We pay particular attention to the surviving samples with $\chi^2 - \chi_{\min}^2 \leq 6.18$, where χ_{\min}^2 denotes the minimum of

Channel	Experiment	Mass range [GeV]	Luminosity
$gg/b\bar{b} \rightarrow H/A \rightarrow \tau^+\tau^-$	ATLAS 8 TeV [43]	90-1000	19.5-20.3 fb ⁻¹
$gg/b\bar{b} \rightarrow H/A \rightarrow \tau^+\tau^-$	CMS 8 TeV [44]	90-1000	19.7 fb ⁻¹
$gg/b\bar{b} \rightarrow H/A \rightarrow \tau^+\tau^-$	CMS 13 TeV [45]	90-3200	12.9 fb ⁻¹
$gg/b\bar{b} \rightarrow H/A \rightarrow \tau^+\tau^-$	CMS 13 TeV [46]	200-2250	36.1 fb ⁻¹
$b\bar{b} \rightarrow H/A \rightarrow \tau^+\tau^-$	CMS 8 TeV [47]	25-80	19.7 fb ⁻¹
$gg/b\bar{b} \rightarrow H/A \rightarrow \tau^+\tau^-$	ATLAS 13 TeV [48]	200-2500	139 fb ⁻¹
$b\bar{b} \rightarrow H/A \rightarrow \mu^+\mu^-$	CMS 8 TeV [49]	25-60	19.7 fb ⁻¹
$pp \rightarrow H/A \rightarrow \gamma\gamma$	ATLAS 13 TeV [50]	200-2400	15.4 fb ⁻¹
$gg \rightarrow H/A \rightarrow \gamma\gamma$	CMS 8+13 TeV [51]	500-4000	12.9 fb ⁻¹
$gg \rightarrow H/A \rightarrow \gamma\gamma + t\bar{t}H/A (H/A \rightarrow \gamma\gamma)$	CMS 8 TeV [52]	80-110	19.7 fb ⁻¹
$gg \rightarrow H/A \rightarrow \gamma\gamma + t\bar{t}H/A (H/A \rightarrow \gamma\gamma)$	CMS 13 TeV [52]	70-110	35.9 fb ⁻¹
$VV \rightarrow H \rightarrow \gamma\gamma + VH (H \rightarrow \gamma\gamma)$	CMS 8 TeV [52]	80-110	19.7 fb ⁻¹
$VV \rightarrow H \rightarrow \gamma\gamma + VH (H \rightarrow \gamma\gamma)$	CMS 13 TeV [52]	70-110	35.9 fb ⁻¹
$gg/VV \rightarrow H \rightarrow W^+W^-$	ATLAS 8 TeV [53]	300-1500	20.3 fb ⁻¹
$gg/VV \rightarrow H \rightarrow W^+W^- (\ell\nu\ell\nu)$	ATLAS 13 TeV [54]	300-3000	13.2 fb ⁻¹
$gg \rightarrow H \rightarrow W^+W^- (\ell\nu qq)$	ATLAS 13 TeV [55]	500-3000	13.2 fb ⁻¹
$gg/VV \rightarrow H \rightarrow W^+W^- (\ell\nu qq)$	ATLAS 13 TeV [56]	200-3000	36.1 fb ⁻¹
$gg/VV \rightarrow H \rightarrow W^+W^- (e\nu\mu\nu)$	ATLAS 13 TeV [57]	200-3000	36.1 fb ⁻¹
$gg/VV \rightarrow H \rightarrow W^+W^-$	CMS 13 TeV [58]	200-3000	35.9 fb ⁻¹
$gg/VV \rightarrow H \rightarrow ZZ$	ATLAS 8 TeV [59]	160-1000	20.3 fb ⁻¹
$gg \rightarrow H \rightarrow ZZ(\ell\nu\nu)$	ATLAS 13 TeV [60]	300-1000	13.3 fb ⁻¹
$gg \rightarrow H \rightarrow ZZ(\nu\nu qq)$	ATLAS 13 TeV [61]	300-3000	13.2 fb ⁻¹
$gg/VV \rightarrow H \rightarrow ZZ(\ell l qq)$	ATLAS 13 TeV [61]	300-3000	13.2 fb ⁻¹
$gg/VV \rightarrow H \rightarrow ZZ(\ell\ell\ell\ell)$	ATLAS 13 TeV [62]	200-3000	14.8 fb ⁻¹
$gg/VV \rightarrow H \rightarrow ZZ(\ell\ell\ell\ell + \ell l\nu\nu)$	ATLAS 13 TeV [63]	200-2000	36.1 fb ⁻¹
$gg/VV \rightarrow H \rightarrow ZZ(\nu\nu qq + \ell l qq)$	ATLAS 13 TeV [64]	300-5000	36.1 fb ⁻¹

TABLE I: The upper limits at 95% C.L. on the production cross-section times branching ratio of $\tau^+\tau^-$, $\mu^+\mu^-$, $\gamma\gamma$, WW , and ZZ considered in the H and A searches at the LHC.

Channel	Experiment	Mass range [GeV]	Luminosity
$gg \rightarrow H \rightarrow hh \rightarrow (\gamma\gamma)(b\bar{b})$	CMS 8 TeV [65]	250-1100	19.7 fb ⁻¹
$gg \rightarrow H \rightarrow hh \rightarrow (b\bar{b})(b\bar{b})$	CMS 8 TeV [66]	270-1100	17.9 fb ⁻¹
$gg \rightarrow H \rightarrow hh \rightarrow (b\bar{b})(\tau^+\tau^-)$	CMS 8 TeV [67]	260-350	19.7 fb ⁻¹
$gg \rightarrow H \rightarrow hh \rightarrow b\bar{b}b\bar{b}$	ATLAS 13 TeV [68]	300-3000	13.3 fb ⁻¹
$gg \rightarrow H \rightarrow hh \rightarrow b\bar{b}b\bar{b}$	CMS 13 TeV [69]	750-3000	35.9 fb ⁻¹
$gg \rightarrow H \rightarrow hh \rightarrow (b\bar{b})(\tau^+\tau^-)$	CMS 13 TeV [70]	250-900	35.9 fb ⁻¹
$pp \rightarrow H \rightarrow hh$	CMS 13 TeV [71]	250-3000	35.9 fb ⁻¹
$gg \rightarrow H \rightarrow hh \rightarrow b\bar{b}ZZ$	CMS 13 TeV [72]	260-1000	35.9 fb ⁻¹
$gg \rightarrow H \rightarrow hh \rightarrow b\bar{b}\tau^+\tau^-$	CMS 13 TeV [73]	1000-3000	139 fb ⁻¹
$gg \rightarrow A \rightarrow hZ \rightarrow (\tau^+\tau^-)(\ell\ell)$	CMS 8 TeV [67]	220-350	19.7 fb ⁻¹
$gg \rightarrow A \rightarrow hZ \rightarrow (b\bar{b})(\ell\ell)$	CMS 8 TeV [74]	225-600	19.7 fb ⁻¹
$gg \rightarrow A \rightarrow hZ \rightarrow (\tau^+\tau^-)Z$	ATLAS 8 TeV [75]	220-1000	20.3 fb ⁻¹
$gg \rightarrow A \rightarrow hZ \rightarrow (b\bar{b})Z$	ATLAS 8 TeV [75]	220-1000	20.3 fb ⁻¹
$gg/b\bar{b} \rightarrow A \rightarrow hZ \rightarrow (b\bar{b})Z$	ATLAS 13 TeV [76]	200-2000	36.1 fb ⁻¹
$gg/b\bar{b} \rightarrow A \rightarrow hZ \rightarrow (b\bar{b})Z$	CMS 13 TeV [77]	225-1000	35.9 fb ⁻¹
$gg \rightarrow A \rightarrow hZ \rightarrow (\tau^+\tau^-)(\ell\ell)$	CMS 13 TeV [78]	220-400	35.9 fb ⁻¹
$gg \rightarrow h \rightarrow AA \rightarrow \tau^+\tau^-\tau^+\tau^-$	ATLAS 8 TeV [79]	4-50	20.3 fb ⁻¹
$pp \rightarrow h \rightarrow AA \rightarrow \tau^+\tau^-\tau^+\tau^-$	CMS 8 TeV [80]	5-15	19.7 fb ⁻¹
$pp \rightarrow h \rightarrow AA \rightarrow (\mu^+\mu^-)(b\bar{b})$	CMS 8 TeV [80]	25-62.5	19.7 fb ⁻¹
$pp \rightarrow h \rightarrow AA \rightarrow (\mu^+\mu^-)(\tau^+\tau^-)$	CMS 8 TeV [80]	15-62.5	19.7 fb ⁻¹
$pp \rightarrow h \rightarrow AA \rightarrow (b\bar{b})(\tau^+\tau^-)$	CMS 13 TeV [81]	15-60	35.9 fb ⁻¹
$pp \rightarrow h \rightarrow AA \rightarrow \tau^+\tau^-\tau^+\tau^-$	CMS 13 TeV [82]	4-15	35.9 fb ⁻¹
$pp \rightarrow h \rightarrow AA \rightarrow \mu^+\mu^-\tau^+\tau^-$	CMS 13 TeV [83]	3.6-21	35.9 fb ⁻¹
$gg \rightarrow A(H) \rightarrow H(A)Z \rightarrow (b\bar{b})(\ell\ell)$	CMS 8 TeV [84]	40-1000	19.8 fb ⁻¹
$gg \rightarrow A(H) \rightarrow H(A)Z \rightarrow (\tau^+\tau^-)(\ell\ell)$	CMS 8 TeV [84]	20-1000	19.8 fb ⁻¹
$gg/b\bar{b} \rightarrow A(H) \rightarrow H(A)Z \rightarrow (b\bar{b})(\ell\ell)$	ATLAS 13 TeV [85]	130-800	36.1 fb ⁻¹
$gg \rightarrow A(H) \rightarrow H(A)Z \rightarrow (b\bar{b})(\ell\ell)$	CMS 13 TeV [86]	30-1000	35.9 fb ⁻¹

TABLE II: The upper limits at 95% C.L. on the production cross-section times branching ratio for the channels of Higgs-pair and a Higgs production in association with Z at the LHC.

χ^2 . These samples correspond to be within the 2σ range in any two-dimension plane of the model parameters when explaining the Higgs data.

- (5) The exclusion limits of searches for additional Higgs bosons. We use `HiggsBounds-4.3.1` [38, 39] to implement the exclusion constraints from the neutral and charged Higgs searches at LEP at 95% confidence level.

Because the b -quark loop and top quark loop have destructive interference contributions to $gg \rightarrow A$ production in the type-II 2HDM, the cross section decreases with an increase of $\tan \beta$, reaches the minimum value for the moderate $\tan \beta$, and is dominated by the b -quark loop for enough large $\tan \beta$. In addition to $\tan \beta$ and m_H , the cross section of $gg \rightarrow H$ depends on $\sin(\beta - \alpha)$. We employ `SusHi` to compute the cross sections for H and A in the gluon fusion and $b\bar{b}$ -associated production at NNLO in QCD [40]. The cross sections of H via vector boson fusion process are deduced from results of the LHC Higgs Cross Section Working Group [41]. We employ `2HDMC` to calculate the branching ratios of the various decay modes of H and A . The searches for the additional Higgs considered by us are listed in Tables I and II. The LHC searches for H^\pm can not impose any constraints on the model for $m_{H^\pm} > 500$ GeV and $1 \leq \tan \beta \leq 25$ [42]. Therefore, we do not consider the constraints from the searches for the heavy charged Higgs.

B. Results and discussions

In Fig. 1, we show $\sin(\beta - \alpha)$ and $\tan \beta$ allowed by the 125 GeV Higgs signal data at the LHC. From Fig. 1, we see that $\tan \beta$ and $\sin(\beta - \alpha)$ have strong correlation due to the constraints of the 125 GeV Higgs data, especially for the case of the wrong sign Yukawa coupling. The wrong sign Yukawa coupling can be achieved only for $\sin(\beta - \alpha) > 0$, and $\tan \beta$ is restricted to be in a very narrow range for a given $\sin(\beta - \alpha)$. For the case of the SM-like coupling, $\sin(\beta - \alpha)$ is required to be in two very narrow ranges of $-1.0 \sim -0.99993$ and $0.994 \sim 1.0$. The $\tan \beta$ is allowed to be as low as 1.0, and its upper bound increases with $|\sin(\beta - \alpha)|$ in the case of the the SM-like Higgs coupling.

Now we examine the parameter space of 2HDMIID using the exclusion limits of searches for additional Higgses at the LHC. In the 2HDMIID, we take the heavy CP-even Higgs H

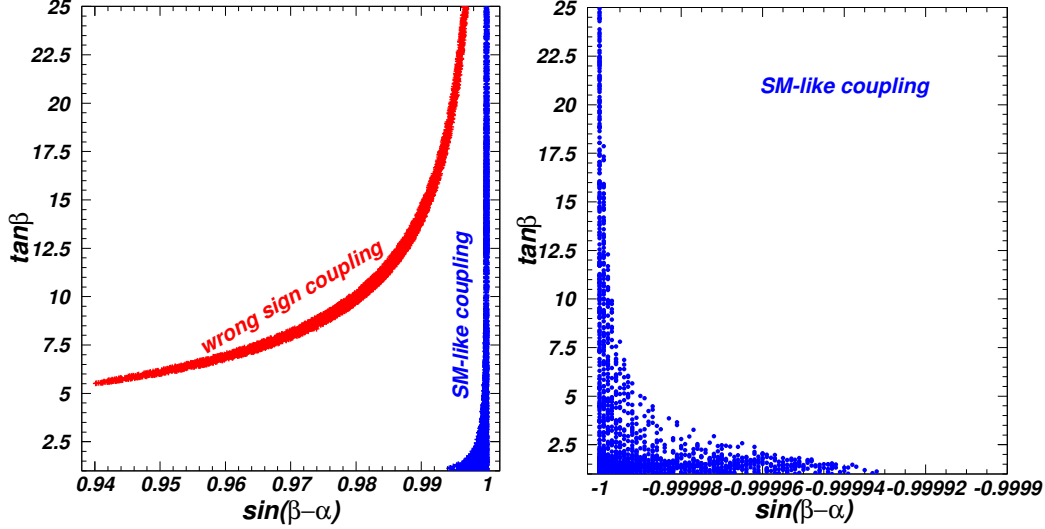


FIG. 1: Scatter plots of $\sin(\beta - \alpha)$ and $\tan\beta$ satisfying the constraints of the 125 GeV Higgs signal data.

as only portal between DM and SM sectors, and the decay $H \rightarrow SS$ opens for $2m_S < m_H$. The decay mode possibly affects the allowed parameter space, but the constraints of the DM observables have to be simultaneously considered. Here we temporarily assume $2m_S > m_H$, and close the $H \rightarrow SS$ decay mode. In the next section, the effects of $H \rightarrow SS$ will be considered by combining the DM observables.

In Fig. 2, we project the surviving samples with the SM-like coupling on the planes of m_H versus $\tan\beta$ and m_H versus $|\sin(\beta - \alpha)|$ after imposing the constraints of pre-LHC (denoting theoretical constraints, electroweak precision data, the flavor observables, R_b , the exclusion limits from searches for Higgs at LEP), the 125 GeV Higgs signal data, and the searches for additional Higgses at the LHC. Note that in the region of $\sin(\beta - \alpha) < 0$, the signal data of the 125 GeV Higgs require $\sin(\beta - \alpha)$ to nearly equal to -1.0, as shown in right panel of Fig. 1. For such case, the couplings of H and A are almost the same as those in the case of $\sin(\beta - \alpha) = 1.0$. Therefore, we do not distinguish the sign of $\sin(\beta - \alpha)$ when discussing the constraints on m_H and m_A from the LHC direct searches.

From Fig. 2, we find the joint constraints of $H/A \rightarrow \tau^+\tau^-$, $A \rightarrow HZ$, $H \rightarrow WW$, ZZ , $\gamma\gamma$, and $H \rightarrow hh$ exclude the whole region of $m_H < 360$ GeV. The $H/A \rightarrow \tau^+\tau^-$ channels impose upper bound on $\tan\beta$ in the whole range of m_H , and allow m_H to vary from 150 GeV to 800 GeV for appropriate values of $\tan\beta$ and $\sin(\beta - \alpha)$. The $A \rightarrow HZ$ channel does not constrain the parameter space of $m_H > 360$ GeV since the branching ratio of $A \rightarrow HZ$

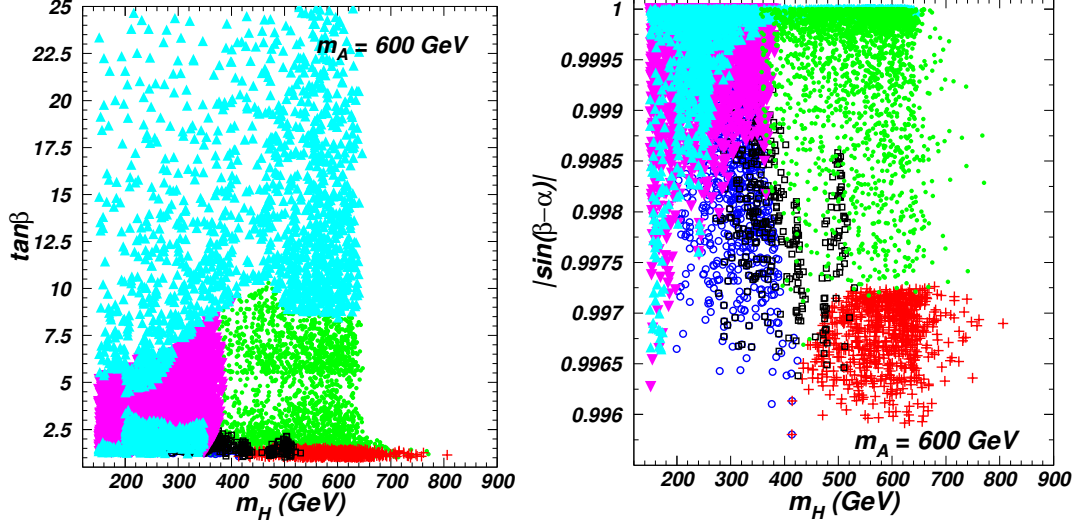


FIG. 2: The surviving samples with the SM-like coupling projected on the planes of m_H versus $\tan\beta$ and m_H versus $|\sin(\beta - \alpha)|$. All the samples are allowed by the constraints of pre-LHC and the 125 GeV Higgs signal data. The triangles (sky blue), circles (royal blue), squares (black), inverted triangles (purple), and pluses (red) are respectively excluded by the $H/A \rightarrow \tau^+\tau^-$, $H \rightarrow WW, ZZ, \gamma\gamma$, $H \rightarrow hh$, $A \rightarrow HZ$, and $A \rightarrow hZ$ channels at the LHC. The bullets (green) are allowed by various LHC direct searches.

rapidly decreases with an increase of m_H . The limits of $A \rightarrow HZ$ channel can be relaxed by a small $|\sin(\beta - \alpha)|$ which suppresses the AHZ coupling.

The $H \rightarrow WW, ZZ, \gamma\gamma, hh$ and $A \rightarrow hZ$ channels impose strong constraints on the regions with small values of $|\sin(\beta - \alpha)|$ and $\tan\beta$ since the couplings of HWW, HZZ, Hhh and AhZ increase with decreasing of $|\sin(\beta - \alpha)|$, and $\sigma(gg \rightarrow H/A)$ is enhanced by the top quark loop for a small $\tan\beta$. In addition, the Fig. 1 shows that the 125 GeV Higgs signal data favor a small $\tan\beta$ for a small $|\sin(\beta - \alpha)|$ in the case of the SM-like coupling. With an increase of m_H , the $H \rightarrow t\bar{t}$ channel opens and enhances the total width of H sizably, so that the constraints from $H \rightarrow WW, ZZ, \gamma\gamma, hh$ channels are relaxed. Different from other channels, the AhZ channel gives the constraints on the region with a large m_H . This is because the width of $A \rightarrow HZ$ decreases with an increase of m_H , and thus $Br(A \rightarrow hZ)$ increases with m_H .

IV. THE DARK MATTER OBSERVABLES

We use FeynRules [87] to generate the model file, which is called by micrOMEGAs [88] to calculate the relic density. In our scenario, the elastic scattering of S on a nucleon receives the contributions of the process with t -channel exchange of H , and the spin-independent cross section between DM and nucleons is given by [89]

$$\sigma_{p(n)} = \frac{\mu_{p(n)}^2}{4\pi m_S^2} [f^{p(n)}]^2, \quad (11)$$

where $\mu_{p(n)} = \frac{m_S m_{p(n)}}{m_S + m_{p(n)}}$,

$$f^{p(n)} = \sum_{q=u,d,s} f_q^{p(n)} \mathcal{C}_{Sq} \frac{m_{p(n)}}{m_q} + \frac{2}{27} f_g^{p(n)} \sum_{q=c,b,t} \mathcal{C}_{Sq} \frac{m_{p(n)}}{m_q}, \quad (12)$$

with $\mathcal{C}_{Sq} = \frac{\lambda_H}{m_H^2} m_q y_H^q$. The values of the form factors $f_q^{p,n}$ and $f_g^{p,n}$ are extracted from micrOMEGAs [88].

The Planck collaboration reported the relic density of cold DM in the universe, $\Omega_c h^2 = 0.1198 \pm 0.0015$ [90]. The XENON1T collaboration reported stringent upper bounds of the spin-independent DM-nucleon cross section [91]. The Fermi-LAT searches for the DM annihilation from dwarf spheroidal satellite galaxies gave the upper limits on the averaged cross sections of the DM annihilation to e^+e^- , $\mu^+\mu^-$, $\tau^+\tau^-$, $u\bar{u}$, $b\bar{b}$, and WW [92].

In Fig. 3, we project the surviving samples on the planes of λ_H versus m_S , m_H versus m_S , and σ_p versus m_S after imposing the constraints of "pre-LHC", the Higgs data at the LHC, the relic density, XENON1T, and Fermi-LAT. The middle panel shows that the $H \rightarrow SS$ decay weakens the constraints of the LHC Higgs data compared to Fig.2. For example, m_H is allowed to be as low as 200 GeV for a light DM. However, the upper bounds of the XENON1T and Fermi-LAT exclude $m_S < 130$ GeV and $m_H < 360$ GeV. In order to obtain the correct relic density, $|\lambda_H|$ is favored to increase with decreasing of m_S . Thus, for a small m_S , a large $|\lambda_H|$ can enhance the spin-independent DM-nucleon cross section and the averaged cross sections of the today DM annihilation to the SM particles, leading that $m_S < 130$ GeV and $m_S < 75$ GeV are respectively excluded by the experimental data of the XENON1T and Fermi-LAT. For $180 \text{ GeV} < m_S < 340 \text{ GeV}$, $|\lambda_H|$ can be allowed to be smaller than 0.01 because of the resonant contribution at $2m_S \sim m_H$.

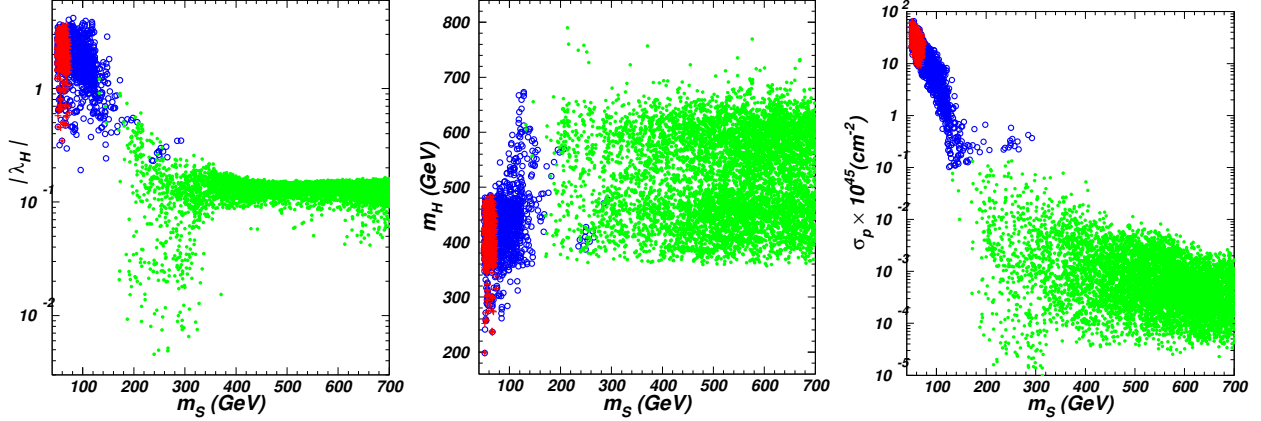


FIG. 3: The surviving samples projected on the planes of m_S versus λ_H , m_S versus m_H , and m_S versus σ_p . All the samples are allowed by the constraints of "pre-LHC", the LHC Higgs data, and the relic density. The circles (royal blue) and pluses (red) are respectively excluded by the experimental data of the XENON1T and Fermi-LAT, while the bullets (green) are allowed.

V. ELECTROWEAK PHASE TRANSITION AND GRAVITATIONAL WAVE

The phase transition can proceed in basically two different ways. In a first-order phase transition, at the critical temperature T_C , the two degenerate minima will be at different points in field space, typically with a potential barrier in between. For a second order (cross-over) transition, the broken and symmetric minimum are not degenerate until they are at the same point in field space. In this paper we focus on the SFOEWPT, which is required by a successful explanation of the observed BAU and can produce primordial GW signals.

A. The thermal effective potential

In order to examine electroweak phase transition (EWPT), we first take h_1 , h_2 , and S_1 as the field configurations, and obtain the field dependent masses of the scalars (h , H , A , H^\pm , S), the Goldstone boson (G , G^\pm), the gauge boson, and fermions. The masses of scalars are given

$$\hat{m}_{h,H,S}^2 = \text{eigenvalues}(\widehat{\mathcal{M}}_P^2), \quad (13)$$

$$\hat{m}_{G,A}^2 = \text{eigenvalues}(\widehat{\mathcal{M}}_A^2), \quad (14)$$

$$\hat{m}_{G^\pm, H^\pm}^2 = \text{eigenvalues}(\widehat{\mathcal{M}}_C^2), \quad (15)$$

$$\begin{aligned}
\widehat{\mathcal{M}}_{P11}^2 &= \frac{3\lambda_1}{2}h_1^2 + \frac{\lambda_{345}}{2}h_2^2 + m_{12}^2 t_\beta - \frac{\lambda_1}{2}v^2 c_\beta^2 - \frac{\lambda_{345}}{2}v^2 s_\beta^2 + \frac{\kappa_1}{2}S_1^2 \\
\widehat{\mathcal{M}}_{P22}^2 &= \frac{3\lambda_2}{2}h_2^2 + \frac{\lambda_{345}}{2}h_1^2 + \frac{m_{12}^2}{t_\beta} - \frac{\lambda_2}{2}v^2 s_\beta^2 - \frac{\lambda_{345}}{2}v^2 c_\beta^2 + \frac{\kappa_2}{2}S_1^2 \\
\widehat{\mathcal{M}}_{P33}^2 &= m_S^2 + \frac{\kappa_1}{2}h_1^2 + \frac{\kappa_2}{2}h_2^2 + \frac{\lambda_S}{2}S_1^2 - \frac{\kappa_1}{2}v^2 c_\beta^2 - \frac{\kappa_2}{2}v^2 s_\beta^2 \\
\widehat{\mathcal{M}}_{P12}^2 &= \widehat{\mathcal{M}}_{P21}^2 = \lambda_{345}h_1h_2 - m_{12}^2 \\
\widehat{\mathcal{M}}_{P13}^2 &= \widehat{\mathcal{M}}_{P31}^2 = \kappa_1 h_1 S_1 \\
\widehat{\mathcal{M}}_{P23}^2 &= \widehat{\mathcal{M}}_{P32}^2 = \kappa_2 h_2 S_1 \\
\widehat{\mathcal{M}}_{A11}^2 &= \frac{\lambda_1}{2}h_1^2 + m_{12}^2 t_\beta - \frac{\lambda_1}{2}v^2 c_\beta^2 - \frac{\lambda_{345}}{2}v^2 s_\beta^2 + \frac{(\lambda_3 + \lambda_4 - \lambda_5)}{2}h_2^2 + \frac{\kappa_1}{2}S_1^2 \\
\widehat{\mathcal{M}}_{A22}^2 &= \frac{\lambda_2}{2}h_2^2 + \frac{m_{12}^2}{t_\beta} - \frac{\lambda_2}{2}v^2 s_\beta^2 - \frac{\lambda_{345}}{2}v^2 c_\beta^2 + \frac{(\lambda_3 + \lambda_4 - \lambda_5)}{2}h_1^2 + \frac{\kappa_2}{2}S_1^2 \\
\widehat{\mathcal{M}}_{A12}^2 &= \widehat{\mathcal{M}}_{A21}^2 = \lambda_5 h_1 h_2 - m_{12}^2 \\
\widehat{\mathcal{M}}_{C11}^2 &= \frac{\lambda_1}{2}h_1^2 + m_{12}^2 t_\beta - \frac{\lambda_1}{2}v^2 c_\beta^2 - \frac{\lambda_{345}}{2}v^2 s_\beta^2 + \frac{\lambda_3}{2}h_2^2 + \frac{\kappa_1}{2}S_1^2 \\
\widehat{\mathcal{M}}_{C22}^2 &= \frac{\lambda_2}{2}h_2^2 + \frac{m_{12}^2}{t_\beta} - \frac{\lambda_2}{2}v^2 s_\beta^2 - \frac{\lambda_{345}}{2}v^2 c_\beta^2 + \frac{\lambda_3}{2}h_1^2 + \frac{\kappa_2}{2}S_1^2 \\
\widehat{\mathcal{M}}_{C12}^2 &= \widehat{\mathcal{M}}_{C21}^2 = \frac{(\lambda_4 + \lambda_5)}{2}h_1h_2 - m_{12}^2,
\end{aligned} \tag{16}$$

where $\lambda_{345} = \lambda_3 + \lambda_4 + \lambda_5$, $c_\beta = \cos \beta$, and $s_\beta = \sin \beta$.

The masses of gauge boson are given

$$\begin{aligned}
\hat{m}_{W^\pm}^2 &= \frac{1}{4}g^2 (h_1^2 + h_2^2), \\
\hat{m}_Z^2 &= \frac{1}{4}(g^2 + g'^2) (h_1^2 + h_2^2), \\
\hat{m}_\gamma^2 &= 0.
\end{aligned} \tag{17}$$

We neglect the contributions of light fermions, and only consider the masses of top quark and bottom quark,

$$\hat{m}_t^2 = \frac{1}{2}y_t^2 h_2^2 / s_\beta^2, \quad \hat{m}_b^2 = \frac{1}{2}y_b^2 h_1^2 / c_\beta^2. \tag{18}$$

where $y_t = \frac{\sqrt{2}m_t}{v}$ and $y_b = \frac{\sqrt{2}m_b}{v}$.

Now we study the effective potential with thermal correction. The thermal effective potential V_{eff} in terms of the classical fields (h_1, h_2, S_1) is composed of four parts:

$$\begin{aligned}
V_{eff}(h_1, h_2, S_1, T) &= V_0(h_1, h_2, S_1) + V_{CW}(h_1, h_2, S_1) + V_{CT}(h_1, h_2, S_1) \\
&\quad + V_T(h_1, h_2, S_1, T) + V_{ring}(h_1, h_2, S_1, T).
\end{aligned} \tag{19}$$

Where V_0 is the tree-level potential, V_{CW} is the Coleman-Weinberg potential, V_{CT} is the counter term, V_T is the thermal correction, and V_{ring} is the resummed daisy corrections. In this paper, we calculate V_{eff} in the Landau gauge.

We obtain the tree-level potential V_0 in terms of their classical fields (h_1, h_2, S_1)

$$\begin{aligned}
\mathcal{V}_0 = & \left[\frac{1}{2}m_{12}^2 t_\beta - \frac{1}{4}\lambda_1 v^2 c_\beta^2 - \frac{1}{4}\lambda_{345} v^2 s_\beta^2 \right] h_1^2 \\
& + \left[\frac{1}{2}m_{12}^2 \frac{1}{t_\beta} - \frac{1}{4}\lambda_2 v^2 s_\beta^2 - \frac{1}{4}\lambda_{345} v^2 c_\beta^2 \right] h_2^2 \\
& + \frac{\lambda_1}{8} h_1^4 + \frac{\lambda_2}{8} h_2^4 - m_{12}^2 h_1 h_2 + \frac{1}{4}\lambda_{345} h_1^2 h_2^2 \\
& + \frac{\kappa_1}{4} h_1^2 S_1^2 + \frac{\kappa_2}{4} h_2^2 S_1^2 + \frac{1}{2}m_S^2 S_1^2 + \frac{1}{24}\lambda_s S_1^4 \\
& - \frac{\kappa_1}{4} v^2 c_\beta^2 S_1^2 - \frac{\kappa_2}{4} v^2 s_\beta^2 S_1^2.
\end{aligned} \tag{20}$$

The Coleman-Weinberg potential in the $\overline{\text{MS}}$ scheme at 1-loop level has the form [93]:

$$V_{CW}(h_1, h_2, S_1) = \sum_i (-1)^{2s_i} n_i \frac{\hat{m}_i^4(h_1, h_2, S_1)}{64\pi^2} \left[\ln \frac{\hat{m}_i^2(h_1, h_2, S_1)}{Q^2} - C_i \right], \tag{21}$$

where $i = h, H, A, H^\pm, S, G, G^\pm, W^\pm, Z, t, b$, and s_i is the spin of particle i . Q is a renormalization scale, and we take $Q^2 = v^2$. The constants $C_i = \frac{3}{2}$ for scalars or fermions and $C_i = \frac{6}{5}$ for gauge bosons. n_i is the number of degree of freedom,

$$\begin{aligned}
n_h = n_H = n_G = n_A = 1, \\
n_{H^\pm} = n_{G^\pm} = 2, \\
n_{W^\pm} = 6, \quad n_Z = 3, \\
n_t = n_b = 12.
\end{aligned} \tag{22}$$

With V_{CW} being included in the potential, the minimization conditions of scalar potential in Eq. (19) and the CP-even mass matrix will be shifted slightly. To maintain the minimization conditions at $T=0$, we add the so-called ‘‘counter-terms’’

$$\begin{aligned}
V_{CT} = & \delta m_1^2 h_1^2 + \delta m_2^2 h_2^2 + \delta \lambda_1 h_1^4 + \delta \lambda_{12} h_1^2 h_2^2 + \delta \lambda_2 h_2^4 \\
& + \delta m_0^2 S_1^2 + \delta \kappa_1 h_1^2 S_1^2 + \delta \kappa_2 h_2^2 S_1^2,
\end{aligned} \tag{23}$$

where the relevant coefficients are determined by

$$\frac{\partial V_{CT}}{\partial h_1} = -\frac{\partial V_{CW}}{\partial h_1}, \quad \frac{\partial V_{CT}}{\partial h_2} = -\frac{\partial V_{CW}}{\partial h_2}, \quad \frac{\partial V_{CT}}{\partial S_1} = -\frac{\partial V_{CW}}{\partial S_1}, \tag{24}$$

$$\begin{aligned}
\frac{\partial^2 V_{\text{CT}}}{\partial h_1 \partial h_1} &= -\frac{\partial^2 V_{\text{CW}}}{\partial h_1 \partial h_1}, & \frac{\partial^2 V_{\text{CT}}}{\partial h_1 \partial h_2} &= -\frac{\partial^2 V_{\text{CW}}}{\partial h_1 \partial h_2}, & \frac{\partial^2 V_{\text{CT}}}{\partial h_2 \partial h_2} &= -\frac{\partial^2 V_{\text{CW}}}{\partial h_2 \partial h_2}, \\
\frac{\partial^2 V_{\text{CT}}}{\partial S_1 \partial S_1} &= -\frac{\partial^2 V_{\text{CW}}}{\partial S_1 \partial S_1}, & \frac{\partial^2 V_{\text{CT}}}{\partial h_1 \partial S_1} &= -\frac{\partial^2 V_{\text{CW}}}{\partial h_1 \partial S_1}, & \frac{\partial^2 V_{\text{CT}}}{\partial h_2 \partial S_1} &= -\frac{\partial^2 V_{\text{CW}}}{\partial h_2 \partial S_1},
\end{aligned} \tag{25}$$

which are evaluated at the EW minimum of $\{h_1 = v_{c\beta}, h_2 = v_{s\beta}, S_1 = 0\}$ on both sides. As a result, the VEVs of h_1, h_2, S_1 and the CP-even mass matrix will not be shifted.

It is a well-known problem that the second derivative of the Coleman-Weinberg potential at $T = 0$ suffers from logarithmic divergences originating from the vanishing Goldstone masses. To solve the divergence problem, we take a straightforward approach of imposing an IR cut-off at $m_{IR}^2 = m_h^2$ for the masses of Goldstone boson of the divergent terms, which gives a good approximation to the exact procedure of on-shell renormalization, as argued in [16].

The thermal contributions V_T to the potential can be written as [94]

$$V_{\text{th}}(h_1, h_2, S_1, T) = \frac{T^4}{2\pi^2} \sum_i n_i J_{B,F} \left(\frac{\hat{m}_i^2(h_1, h_2, S_1)}{T^2} \right), \tag{26}$$

where $i = h, H, A, H^\pm, S, G, G^\pm, W^\pm, Z, t, b$, and the functions $J_{B,F}$ are

$$J_{B,F}(y) = \pm \int_0^\infty dx x^2 \ln \left[1 \mp \exp \left(-\sqrt{x^2 + y} \right) \right]. \tag{27}$$

Finally, the thermal corrections with resummed ring diagrams are given [95, 96]

$$V_{\text{ring}}(h_1, h_2, S_1, T) = -\frac{T}{12\pi} \sum_i n_i \left[(\bar{M}_i^2(h_1, h_2, S_1, T))^{\frac{3}{2}} - (\hat{m}_i^2(h_1, h_2, S_1, T))^{\frac{3}{2}} \right], \tag{28}$$

where $i = h, H, A, H^\pm, S, G, G^\pm, W_L^\pm, Z_L, \gamma_L$. The W_L^\pm, Z_L , and γ_L are the longitudinal gauge bosons with $n_{W_L^\pm} = 2, n_{Z_L} = n_{\gamma_L} = 1$. The thermal Debye masses $\bar{M}_i^2(h_1, h_2, S_1, T)$ are the eigenvalues of the full mass matrix,

$$\bar{M}_i^2(h_1, h_2, T) = \text{eigenvalues} \left[\widehat{\mathcal{M}}_X^2(h_1, h_2) + \Pi_X(T) \right], \tag{29}$$

where $X = P, A, C$. Π_X are given by

$$\begin{aligned}
\Pi_{P11} &= \left[\frac{9g^2}{2} + \frac{3g'^2}{2} + \frac{6y_b^2}{c_\beta^2} + 6\lambda_1 + 4\lambda_3 + 2\lambda_4 + \kappa_1 \right] \frac{T^2}{24} \\
\Pi_{P22} &= \left[\frac{9g^2}{2} + \frac{3g'^2}{2} + \frac{6y_t^2}{s_\beta^2} + 6\lambda_2 + 4\lambda_3 + 2\lambda_4 + \kappa_2 \right] \frac{T^2}{24} \\
\Pi_{P33} &= [4\kappa_1 + 4\kappa_2 + \lambda_S] \frac{T^2}{24} \\
\Pi_{P13} &= \Pi_{P31} = \Pi_{P23} = \Pi_{P32} = 0 \\
\Pi_{A11} &= \Pi_{C11} = \Pi_{P11} \\
\Pi_{A22} &= \Pi_{C22} = \Pi_{P22} \\
\Pi_{A12} &= \Pi_{A21} = \Pi_{C12} = \Pi_{C21} = 0.
\end{aligned} \tag{30}$$

The physical mass of the longitudinally polarized W boson is

$$\bar{M}_{W_L^\pm}^2 = \frac{1}{4}g^2(h_1^2 + h_2^2) + 2g^2T^2. \tag{31}$$

The physical mass of the longitudinally polarized Z and γ boson

$$\bar{M}_{Z_L, \gamma_L}^2 = \frac{1}{8}(g^2 + g'^2)(h_1^2 + h_2^2) + (g^2 + g'^2)T^2 \pm \Delta, \tag{32}$$

with

$$\Delta^2 = \frac{1}{64}(g^2 + g'^2)^2(h_1^2 + h_2^2 + 8T^2)^2 - g^2g'^2T^2(h_1^2 + h_2^2 + 4T^2). \tag{33}$$

B. Calculation of electroweak phase transition and gravitational wave

In a first-order cosmological phase transition, bubbles nucleate and expand, converting the high-temperature phase into the low-temperature one. The bubble nucleation rate per unit volume at finite temperature is given by [97–99]

$$\Gamma \approx A(T)e^{-S_E(T)}, \tag{34}$$

where $A(T) \sim T^4$ is a prefactor and S_E is the Euclidean action

$$S_E(T) = \frac{S_3(T)}{T} = \int dx^3 \left[\frac{1}{2} \left(\frac{d\phi}{dr} \right)^2 + V(\phi, T) \right]. \tag{35}$$

At the nucleation temperature T_n , the thermal tunneling probability for bubble nucleation per horizon volume and per horizon time is of order one, and the conventional condition is

$\frac{S_3(T)}{T} \approx 140$. The bubbles nucleated within one Hubble patch proceed to expand and collide, until the entire volume is filled with the true vacuum.

There are two key parameters characterizing the dynamics of the EWPT, β and α . β describes roughly the inverse time duration of the strong first order phase transition,

$$\frac{\beta}{H_n} = T \frac{d(S_3(T)/T)}{dT} \Big|_{T=T_n}, \quad (36)$$

where H_n is the Hubble parameter at the bubble nucleation temperature T_n . α is defined as the vacuum energy released from the phase transition normalized by the total radiation energy density ρ_R at T_n ,

$$\alpha = \frac{\Delta\rho}{\rho_R} = \frac{\Delta\rho}{\pi^2 g_* T_n^4 / 30}, \quad (37)$$

where g_* is the effective number of relativistic degrees of freedom. We use the numerical package CosmoTransitions [100] and PhaseTracer [101] to analyze the phase transition and computes quantities related to cosmological phase transition.

In a radiation-dominated Universe, there are three sources of GW production at a EWPT: bubble collisions, in which the localized energy density generates a quadrupole contribution to the stress-energy tensor, which in turn gives rise to GW, plus sound waves in the plasma and magnetohydrodynamic (MHD) turbulence. The total resultant energy density spectrum can be approximately given as,

$$\Omega_{\text{GW}} h^2 \simeq \Omega_{\text{col}} h^2 + \Omega_{\text{sw}} h^2 + \Omega_{\text{turb}} h^2. \quad (38)$$

Recent studies show that the energy deposited in the bubble walls is negligible, despite the possibility that the bubble walls can run away in some circumstances [102]. Therefore, although a bubble wall can reach relativistic speed, its contribution to GW can generally be neglected [103, 104]. Therefore, in the following discussions we do not include the contribution from bubble collision Ω_{col} .

The GW spectrum from the the sound waves can be obtained by fitting to the result of numerical simulations [105],

$$\begin{aligned} \Omega_{\text{sw}} h^2 &= 2.65 \times 10^{-6} \left(\frac{H_n}{\beta} \right) \left(\frac{\kappa_v \alpha}{1 + \alpha} \right)^2 \left(\frac{100}{g_*} \right)^{1/3} v_w \\ &\times \left(\frac{f}{f_{\text{sw}}} \right)^3 \left(\frac{7}{4 + 3(f/f_{\text{sw}})^2} \right)^{7/2}, \end{aligned} \quad (39)$$

where f_{sw} is the present peak frequency of the spectrum,

$$f_{\text{sw}} = 1.9 \times 10^{-5} \frac{1}{v_w} \left(\frac{\beta}{H_n} \right) \left(\frac{T_n}{100\text{GeV}} \right) \left(\frac{g_*}{100} \right)^{1/6} \text{Hz}. \quad (40)$$

v_w is the wall velocity, and the factor κ_v is the fraction of latent heat transformed into the kinetic energy of the fluid. κ_v and v_w are difficult to compute, and involves certain assumptions regarding the dynamics of the bubble walls. On the other hand, successful electroweak baryogenesis scenarios favor lower wall velocity $v_w \leq 0.15 - 0.3$ [106], which allows the effective diffuse of particle asymmetries near the bubble wall front. In Ref. [107], however, it is pointed out that the relevant velocity for electroweak baryogenesis is not really v_w , but the relative velocity between the bubble wall and the plasma in the deflagration front. As a result, the electroweak baryogenesis is not necessarily impossible even in the case with large v_w . Therefore, in this paper we take two different cases of v_w and κ_v [108]:

- For small wall velocity: $v_w = 0.3$ and

$$\kappa_v \simeq v_w^{6/5} \frac{6.9\alpha}{1.36 - 0.037\sqrt{\alpha} + \alpha}. \quad (41)$$

- For very large wall velocity: $v_w = 0.9$ and

$$\kappa_v \simeq \frac{\alpha}{0.73 + 0.083\sqrt{\alpha} + \alpha}. \quad (42)$$

Considering Kolmogorov-type turbulence as proposed in Ref. [109], the GW spectrum from the MHD turbulence has the form [110, 111],

$$\begin{aligned} \Omega_{\text{turb}} h^2 &= 3.35 \times 10^{-4} \left(\frac{H_n}{\beta} \right) \left(\frac{\kappa_{\text{turb}} \alpha}{1 + \alpha} \right)^{3/2} \left(\frac{100}{g_*} \right)^{1/3} v_w \\ &\times \frac{(f/f_{\text{turb}})^3}{[1 + (f/f_{\text{turb}})]^{11/3} (1 + 8\pi f/h_n)}, \end{aligned} \quad (43)$$

with the red-shifted Hubble rate at GW generation

$$h_n = 1.65 \times 10^{-5} \left(\frac{T_n}{100\text{GeV}} \right) \left(\frac{g_*}{100} \right)^{1/6} \text{Hz}. \quad (44)$$

The peak frequency f_{turb} is given by

$$f_{\text{turb}} = 2.7 \times 10^{-5} \frac{1}{v_w} \left(\frac{\beta}{H_n} \right) \left(\frac{T_n}{100\text{GeV}} \right) \left(\frac{g_*}{100} \right)^{1/6} \text{Hz}. \quad (45)$$

The energy fraction transferred to the MHD turbulence κ_{turb} can vary between 5% to 10% of κ_v [105]. Here we take $\kappa_{\text{turb}} = 0.1\kappa_v$.

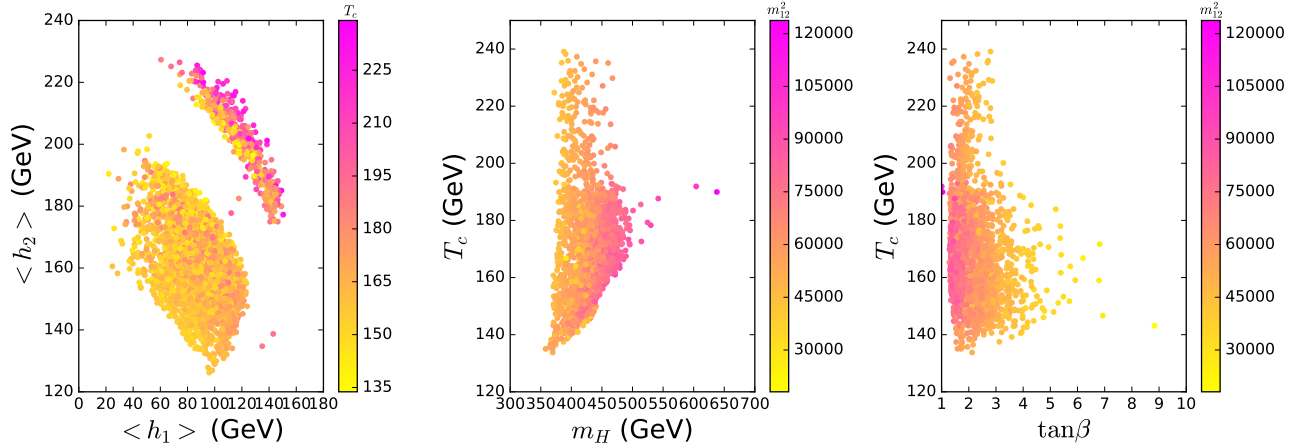


FIG. 4: The surviving samples projected on the planes of $\langle h_1 \rangle$ versus $\langle h_2 \rangle$, T_c versus m_H , and T_c versus $\tan\beta$. All the samples achieve a SFOEWPT.

For both sound wave and turbulence contribution as shown in Eq. (40) and Eq. (43), the amplitudes of the GW spectra are proportional to v_w and the peak frequencies shift as $1/v_w$. Therefore, one changes in the wall velocity approximately have an order one effect on the spectrum and peak frequencies.

C. Results and discussions

The strength of the electroweak phase transition is quantified as

$$\xi_c = \frac{v_c}{T_c} \quad (46)$$

with $v_c = \sqrt{\langle h_1 \rangle^2 + \langle h_2 \rangle^2}$ at critical temperature T_c . The global minimum of potential has $\langle A \rangle = 0$ because of the CP-conserving case. In order to avoid washing out the baryon number generated during the phase transition, a SFOEWPT is required and the conventional condition is $\xi_c \geq 1$.

After imposing the constraints of "pre-LHC", the LHC Higgs data, the relic density, XENON1T, and Fermi-LAT, we scan over the parameter space in the previous selected scenario. We find some surviving samples which can achieve a SFOEWPT, and these samples are projected in Fig. 4 and Fig. 5. For all the surviving samples, at T_c the two degenerate minima of potential are respectively at $(\langle h_1 \rangle, \langle h_2 \rangle, 0)$ and $(0, 0, 0)$. In the process of EWPT, $\langle S_1 \rangle$ always has no VEV.

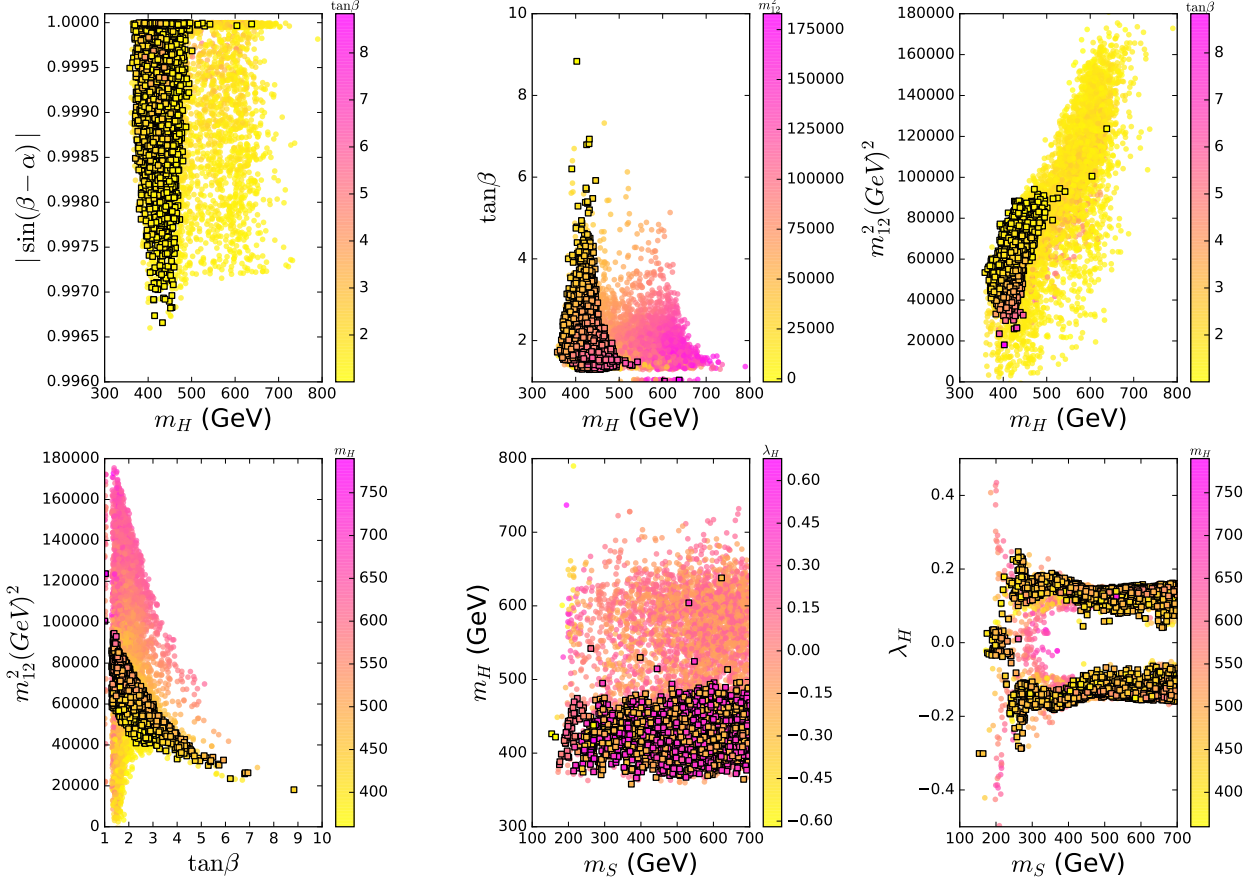


FIG. 5: The surviving samples projected on the planes of $|\sin(\beta - \alpha)|$, $\tan\beta$, m_{12}^2 versus m_H , m_{12}^2 versus $\tan\beta$, and m_S versus m_H , λ_H . All the samples are allowed by the constraints of "pre-LHC", the LHC Higgs data, and the DM observables. The squares achieve a SFOEWPT, and bullets fail.

From Fig. 4, we find that $\langle h_1 \rangle$ and $\langle h_2 \rangle$ can vary in the ranges of 20 GeV \sim 150 GeV and 125 GeV \sim 230 GeV with T_c varying from 134 GeV to 240 GeV. T_c tends to increase with m_H , and has a relative small value for a large $\tan\beta$. It should also be noted that the relic abundance of the DM is achieved by the thermal freeze-out in the early universe when the temperature was about $T \sim m_S/25$. In the model, T_c is much larger than $m_S/25$ for $50 \text{ GeV} < m_S < 700 \text{ GeV}$. Therefore, the EWPT hardly affects the thermal freeze-out process of DM.

From Fig. 5, we find that a SFOEWPT favors a small m_H , namely a large mass splitting between m_H and m_A , which is consistent with Refs. [17, 18]. Most of samples lie in the region of $m_H < 500 \text{ GeV}$, and there are several samples with $m_H > 500 \text{ GeV}$ when $|\sin(\beta - \alpha)|$ is very closed to 1.0. Also a SFOEWPT favors m_{12}^2 to increase with m_H and decrease with

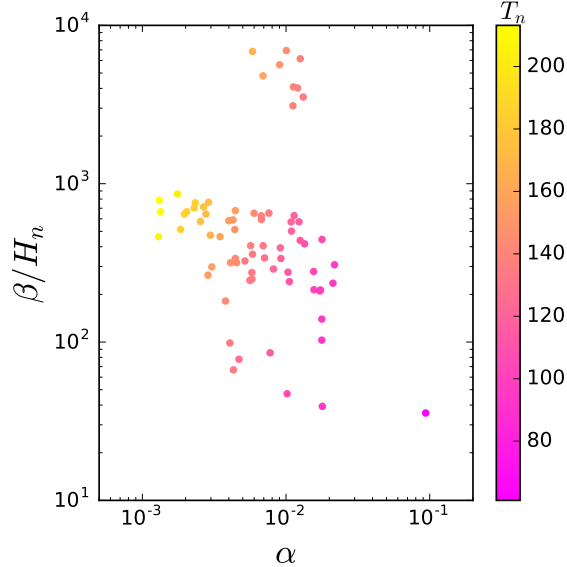


FIG. 6: The parameters α and β/H_n characterizing the dynamics of the SFOEWPT.

an increase of $\tan \beta$. There is a relative strong correlation between m_{12}^2 and $\tan \beta$, and m_{12}^2 is imposed upper and lower bounds for a given $\tan \beta$. With an increase of $\tan \beta$, m_{12}^2 is stringently restricted by the theoretical constraints and the LHC Higgs data, leading that it is difficult to achieve a SFOEWPT. Thus, most of samples lie in the region of small $\tan \beta$. The requirement of a SFOEWPT is not sensitive to m_S , and disfavors $|\lambda_H| > 0.3$.

Now we examine two key parameters α and β/H_n which characterize the dynamics of the SFOEWPT, and govern the strength of GW spectra. A larger α and smaller β/H_n can lead to stronger GW signals. In addition to the conditions of the successful bubble nucleations, we require

$$\xi_n = \frac{v_n}{T_n} \geq 1 \quad (47)$$

with $v_n = \sqrt{\langle h_1 \rangle^2 + \langle h_2 \rangle^2}$ at the nucleation temperature T_n . In fact, this is a more precise condition of SFOEWPT than $\xi_c \geq 1$. Also note that there generically exists a difficulty for solving bounce solution in a very thin-walled bubble, including the package CosmoTransitions [112]. Therefore, we will neglect the samples with very thin-walled bubble. Consider the constraints discussed above, we find some surviving samples, and the corresponding α and β/H_n are shown in Fig. 6.

The β/H_n may characterize the inverse time duration of the EWPT. A small β/H_n means a long EWPT, and gives strong GW signals. For the GW coming from the sound waves in the plasma, the GW signal will continue being generated and the energy density of the GW

	BP1	BP2
$\sin(\beta - \alpha)$	0.9998	0.9991
$\tan \beta$	1.95	1.87
m_H (GeV)	369.55	387.97
m_{H^\pm} (GeV)	620.8	618.31
m_{12}^2 (GeV) ²	53049.1	53649.1
m_S (GeV)	479.2	501.7
λ_H	0.133	-0.129
λ_S	12.3	10.93
T_c (GeV)	135.7	160.0
T_n (GeV)	61.0	95.0
β/H_n	35.6	102.8
α	0.094	0.018

TABLE III: Input and output parameters for two benchmark points for fixed $m_h=125$ GeV, $m_A=600$ GeV and $\lambda_h = 0$.

is thus proportional to the duration of the EWPT if the mean square fluid velocity of the plasma is non-negligible [105]. In addition, a large β/H_n can enhance the peak frequency of the GW spectra. The parameter α describes the amount of energy released during the EWPT, and therefore a large α leads to strong GW signals.

We pick out two benchmark points (BPs), and examine the corresponding GW spectra. Table III shows the input and output parameters of the BPs. Their phase histories are exhibited in Fig. 7 on field configurations versus temperature plane. The field configuration S_1 is not shown as the minima at any temperatures locate at $\langle S_1 \rangle = 0$. In Fig. 8, we show predicted GW spectra for our BPs along with expected sensitivities of various future interferometer experiments, and find that the amplitudes of the GW spectra reach the sensitivities of LISA, TianQin, BBO, DECIGO, UDECIGO for BP1 (UDECIGO for BP2).

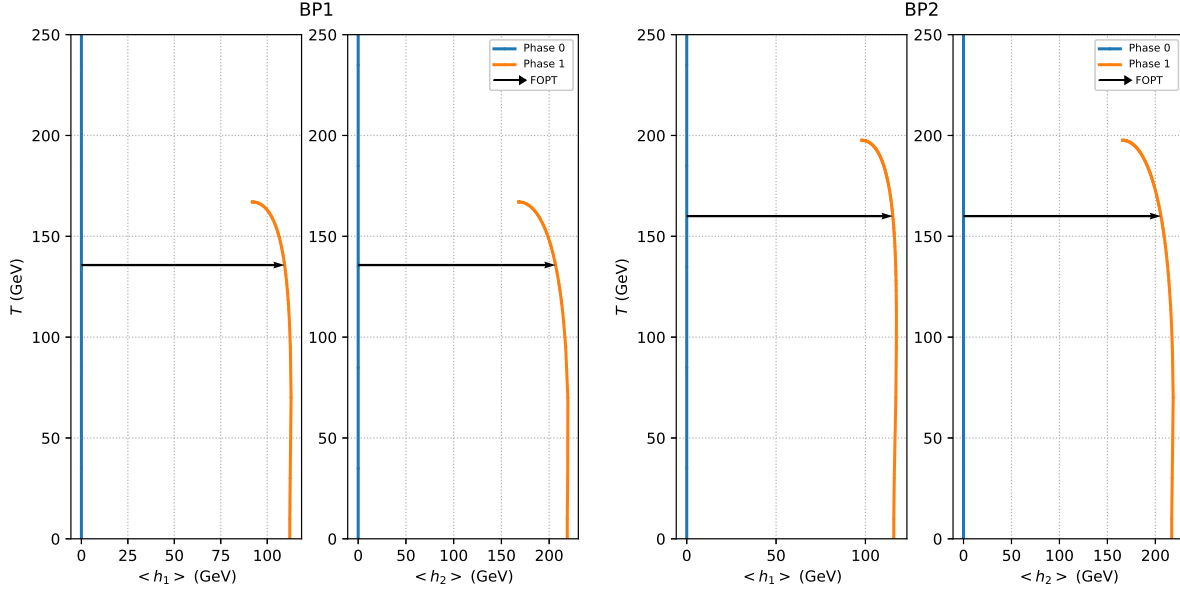


FIG. 7: Phase structures for BP1 (left) and BP2 (right). The lines show the field configurations at a particular minimum as a function of temperature. The arrows indicate that at that temperature (T_C) the two phases linked by the arrows are degenerate, and can achieve the first order phase transition (FOPT).

VI. CONCLUSION

We examine the status of the 2HDMIID confronted with the recent LHC Higgs data, the DM observables and SFOEWPT, and discuss the detectability of GW at the future GW detectors. We choose the heavy CP-even Higgs H as the only portal between the DM and SM sectors, and focus on the case of the 125 GeV Higgs with the SM-like coupling. We find that for $m_A = 600$ GeV, $m_S < 130$ GeV and $m_H < 360$ GeV are excluded by the joint constraints of the 125 GeV Higgs signal data, the searches for additional Higgs via $H/A \rightarrow \tau^+\tau^-$, $A \rightarrow HZ$, $H \rightarrow WW$, ZZ , $\gamma\gamma$, hh at the LHC as well as the relic density, XENON1T.

A SFOEWPT can be achieved in the many regions of $m_H < 500$ GeV and $m_A = 600$ GeV, favors a small $\tan\beta$, and is not sensitive to the mass of DM. We find the benchmark points for which the predicted GW spectra can reach the sensitivities of LISA, TianQin, BBO, DECIGO, and UDECIGO.

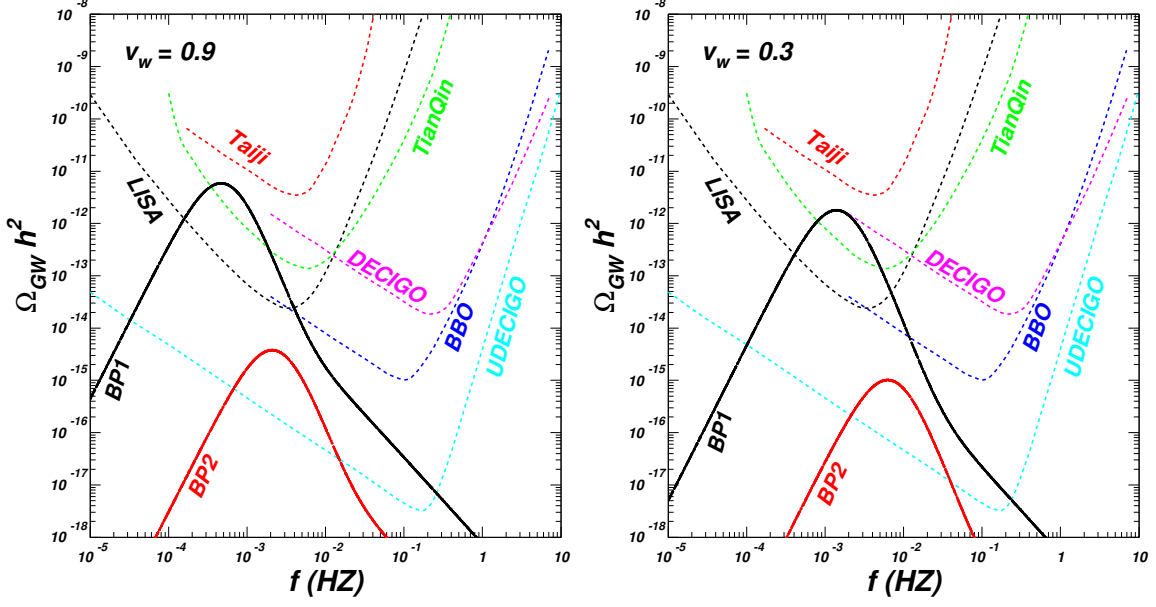


FIG. 8: Gravitational wave spectra for BP1 and BP2.

Acknowledgment

We thank L. Bian, Wei Chao and Huai-Ke Guo for helpful discussions. This work was supported by the National Natural Science Foundation of China under grant 11975013, by the Natural Science Foundation of Shandong province (ZR2017MA004 and ZR2017JL002), and by the ARC Centre of Excellence for Particle Physics at the Tera-scale under the grant CE110001004. This work is also supported by the Project of Shandong Province Higher Educational Science and Technology Program under Grants No. 2019KJJ007.

-
- [1] T. D. Lee, Phys. Rev. D **8**, 1226 (1973).
 - [2] H. E. Haber, G. L. Kane and T. Sterling, Nucl. Phys. B **161**, 493 (1979).
 - [3] J. F. Donoghue and L. F. Li, Phys. Rev. D **19**, 945 (1979).
 - [4] X.-G. He, T. Li, X.-Q. Li, J. Tandean, H.-C. Tsai, Phys. Rev. D **79**, 023521 (2009).
 - [5] X.-G. He, J. Tandean, Phys. Rev. D **88**, 013020 (2013).
 - [6] Y. Cai, T. Li, Phys. Rev. D **88**, 115004 (2013).
 - [7] L. Wang, X.-F. Han, Phys. Lett. B **739**, 416-420 (2014).
 - [8] A. Drozd, B. Grzadkowski, J. F. Gunion, Y. Jiang, JHEP **1411**, 105 (2014).

- [9] X.-G. He, J. Tandean, JHEP **1612**, 074 (2016).
- [10] T. Alanne, K. Kainulainen, K. Tuominen, V. Vaskonen, JCAP **1608**, 057 (2016).
- [11] L. Wang, R. Shi, X.-F. Han, Phys. Rev. D **96**, 115025 (2017).
- [12] N. Chen, Z. Kang, J. Li, Phys. Rev. D **95**, 015003 (2017).
- [13] L. Wang, X.-F. Han, B. Zhu, Phys. Rev. D **98**, 035024 (2018).
- [14] S. Baum, N. R. Shah, JHEP **12**, 044 (2018).
- [15] A. I. Bochkarev, S. V. Kuzmin and M. E. Shaposhnikov, Phys. Lett. B **244**, 275 (1990); J. M. Cline, P.-A. Lemieux, Phys. Rev. D **55**, 3873 (1997); G. C. Dorsch, S. J. Huber and J. M. No, JHEP **1310**, 029 (2013); G. C. Dorsch, S. J. Huber, K. Mimasu and J. M. No, Phys. Rev. Lett. **113**, 211802 (2014); N. Chen, T. Li, Z. Teng, Y. Wu, arXiv:2006.06913; R. Zhou, L. Bian, arXiv:2001.01237; R. Zhou, L. Bian, H.-K Guo, Phys. Rev. D **101**, 091903 (2020); X. Wang, F. Huang, X. Zhang, Phys. Rev. D **101**, 015015 (2020); JCAP **05**, 045 (2020).
- [16] J. M. Cline, K. Kainulainen and M. Trott, JHEP **1111**, 089 (2011).
- [17] P. Basler, M. Krause, M. Muhlleitner, J. Wittbrodt and A. Wlotzka, JHEP **1702**, 121 (2017).
- [18] J. Bernon, L. Bian and Y. Jiang, JHEP **1805**, 151 (2018).
- [19] A. D. Sakharov, Pisma Zh. Eksp. Teor. Fiz. **5**, 32 (1967) [JETP Lett. **5**, 24 (1967)] [Sov. Phys. Usp. **34**, no. 5, 392 (1991)] [Usp. Fiz. Nauk **161**, no. 5, 61 (1991)].
- [20] M. Kamionkowski, A. Kosowsky and M. S. Turner, Phys. Rev. D **49**, 2837 (1994).
- [21] LISA Collaboration, H. Audley et al., “Laser Interferometer Space Antenna,” arXiv:1702.00786.
- [22] X. Gong et al., “Descopes of the ALIA mission,” J. Phys. Conf. Ser. **610**, 012011 (2015).
- [23] TianQin Collaboration, J. Luo et al., “TianQin: a space-borne gravitational wave detector,” Class. Quant. Grav. **33**, 035010 (2016).
- [24] K. Yagi and N. Seto, “Detector configuration of DECIGO/BBO and identification of cosmological neutron-star binaries,” Phys. Rev. D **83**, 044011 (2011).
- [25] H. Kudoh, A. Taruya, T. Hiramatsu, and Y. Himemoto, “Detecting a gravitational-wave background with next-generation space interferometers,” Phys. Rev. D **73**, 064006 (2006).
- [26] R. A. Battye, G. D. Brawn, A. Pilaftsis, JHEP **1108**, 020 (2011).
- [27] Heavy Flavor Averaging Group, Eur. Phys. Jour. C **77**, 895 (2017); M. Misiak, M. Steinhauser, Eur. Phys. Jour. C **77**, 201 (2017).

- [28] F. Kling, J. M. No, S. Su, JHEP **1609**, 093 (2016).
- [29] L. Wang, F. Zhang, X.-F. Han, Phys. Rev. D **95**, 115014 (2017).
- [30] L. Wang, H.-X. Wang, X.-F. Han, Comput. Phys. Commun. **44**, 073101 (2020).
- [31] D. Eriksson, J. Rathsmann, O. Stål, Comput. Phys. Commun. **181**, 189 (2010).
- [32] M. Tanabashi et al., [Particle Data Group], Phys. Rev. D **98**, 030001 (2018).
- [33] F. Mahmoudi, Comput. Phys. Commun. **180**, 1579-1673 (2009).
- [34] C. Q. Geng and J. N. Ng, Phys. Rev. D **38**, 2857 (1988) [Erratum-ibid. D 41, 1715 (1990)].
- [35] H. E. Haber, H. E. Logan, Phys. Rev. D **62**, 015011 (2010).
- [36] G. Degrossi, P. Slavich, Phys. Rev. D **81**, 075001 (2010).
- [37] J. Bernon, B. Dumont, S. Kraml, Phys. Rev. D **90**, 071301 (2014); S. Kraml, T. Q. Loc, D. T Nhung, L. D. Ninh, arXiv:1908.03952.
- [38] P. Bechtle, O. Brein, S. Heinemeyer, G. Weiglein, K. E. Williams, Comput. Phys. Commun. **181**, 138-167 (2010).
- [39] P. Bechtle, O. Brein, S. Heinemeyer, O. Stål, T. Stefaniak, G. Weiglein, K. E. Williams, Eur. Phys. Jour. C **74**, 2693 (2014).
- [40] R. V. Harlander, S. Liebler, H. Mantler, Comput. Phys. Commun. **184**, 1605 (2013).
- [41] S. Heinemeyer et al. [LHC Higgs Cross Section Working Group Collaboration], arXiv:1307.1347.
- [42] S. Moretti, arXiv:1612.02063.
- [43] ATLAS Collaboration, G. Aad *et al.*, “Search for neutral Higgs bosons of the minimal supersymmetric standard model in pp collisions at $\sqrt{s} = 8$ TeV with the ATLAS detector,” JHEP **11**, 056 (2014).
- [44] CMS Collaboration, “Search for additional neutral Higgs bosons decaying to a pair of tau leptons in pp collisions at $\sqrt{s} = 7$ and 8 TeV,” CMS-PAS-HIG-14-029.
- [45] CMS Collaboration, “Search for a neutral MSSM Higgs Boson decaying into $\tau\tau H/A$ with 12.9 fb⁻¹ of data at $\sqrt{s}= 13$ TeV,” CMS-PAS-HIG-16-037.
- [46] ATLAS Collaboration, “Search for additional heavy neutral Higgs and gauge bosons in the ditau final state produced in 36 fb⁻¹ of pp collisions at $\sqrt{s}= 13$ TeV with the ATLAS detector,” JHEP **1801**, 055 (2018).
- [47] CMS Collaboration, “Search for a low-mass pseudoscalar Higgs boson produced in association with a $b\bar{b}$ pair in pp collisions at $\sqrt{s} = 8$ TeV,” Phys. Lett. B **758**, 296-320 (2016).

- [48] ATLAS Collaboration, “Search for heavy Higgs bosons decaying into two tau leptons with the ATLAS detector using p p collisions at $\sqrt{s} = 13$ TeV,” arXiv:2002.12223.
- [49] CMS Collaboration, “Search for a light pseudoscalar Higgs boson produced in association with bottom quarks in pp collisions at $\sqrt{s} = 8$ TeV,” CMS-HIG-15-009.
- [50] ATLAS Collaboration, “Search for scalar diphoton resonances with 15.4 fb^{-1} of data collected at $\sqrt{s} = 13$ TeV in 2015 and 2016 with the ATLAS detector,” ATLAS-CONF-2016-059.
- [51] CMS Collaboration, “Search for resonant production of high mass photon pairs using 12.9 fb^{-1} of proton-proton collisions at $\sqrt{s} = 13$ TeV and combined interpretation of searches at 8 and 13 TeV,” CMS-PAS-EXO-16-027.
- [52] CMS Collaboration, “Search for new resonances in the diphoton final state in the mass range between 70 and 110 GeV in pp collisions at $\sqrt{s} = 8$ and 13 TeV,” CMS-PAS-HIG-17-013.
- [53] ATLAS Collaboration, G. Aad *et al.*, “Search for a high-mass Higgs boson decaying to a W boson pair in *pp* collisions at $\sqrt{s} = 8$ TeV with the ATLAS detector,” JHEP **01**, (2016) 032.
- [54] ATLAS collaboration, “Search for a high-mass Higgs boson decaying to a pair of W bosons in pp collisions at $\sqrt{s} = 13$ TeV with the ATLAS detector,” ATLAS-CONF-2016-074.
- [55] ATLAS Collaboration, “Search for diboson resonance production in the $\ell\nu qq$ final state using p p collisions at $\sqrt{s} = 13$ TeV with the ATLAS detector at the LHC,” ATLAS-CONF-2016-062.
- [56] ATLAS Collaboration, “Search for WW/WZ resonance production in $\ell\nu qq$ final states in pp collisions at $\sqrt{s} = 13$ TeV with the ATLAS detector,” arXiv:1710.07235.
- [57] ATLAS Collaboration, “Search for heavy resonances decaying into WW in the $e\nu\mu\nu$ final state in pp collisions $\sqrt{s} = 13$ TeV with the ATLAS detector,” Eur. Phys. Jour. C **78**, 24 (2018).
- [58] CMS Collaboration, “Search for a heavy Higgs boson decaying to a pair of W bosons in proton-proton collisions at $\sqrt{s} = 13$ TeV,” arXiv:1912.01594.
- [59] ATLAS Collaboration, G. Aad *et al.*, “Search for an additional, heavy Higgs boson in the $H \rightarrow ZZ$ decay channel at $\sqrt{s} = 8$ TeV in *pp* collision data with the ATLAS detector,” Eur. Phys. Jour. C **76**, 45 (2016).
- [60] ATLAS Collaboration, “Search for new phenomena in the $Z(\rightarrow \ell\ell) + E_{\text{T}}^{\text{miss}}$ final state at $\sqrt{s} = 13$ TeV with the ATLAS detector,” ATLAS-CONF-2016-056.
- [61] ATLAS Collaboration, “Searches for heavy ZZ and ZW resonances in the $\ell\ell qq$ and $\nu\nu qq$ final

- states in pp collisions at $\sqrt{s} = 13$ TeV with the ATLAS detector,” ATLAS-CONF-2016-082.
- [62] ATLAS Collaboration, “Study of the Higgs boson properties and search for high-mass scalar resonances in the $H \rightarrow ZZ^* \rightarrow 4\ell$ decay channel at $\sqrt{s} = 13$ TeV with the ATLAS detector,” ATLAS-CONF-2016-079.
- [63] ATLAS Collaboration, “Search for heavy ZZ resonances in the $\ell^+\ell^-\ell^+\ell^-$ and $\ell^+\ell^-\nu\nu$ final states using proton proton collisions at $\sqrt{s} = 13$ TeV with the ATLAS detector,” arXiv:1712.06386.
- [64] ATLAS Collaboration, “Searches for heavy ZZ and ZW resonances in the $\ell\ell qq$ and $\nu\nu qq$ final states in pp collisions at $\sqrt{s} = 13$ TeV with the ATLAS detector,” arXiv:1708.09638.
- [65] CMS Collaboration, V. Khachatryan *et al.*, “Search for two Higgs bosons in final states containing two photons and two bottom quarks,” Phys. Rev. D **94**, 052012 (2016).
- [66] CMS Collaboration, V. Khachatryan *et al.*, “Search for resonant pair production of Higgs bosons decaying to two bottom quark–antiquark pairs in proton–proton collisions at 8 TeV,” Phys. Lett. B **749**, 560-582 (2015).
- [67] CMS Collaboration, V. Khachatryan *et al.*, “Searches for a heavy scalar boson H decaying to a pair of 125 GeV Higgs bosons hh or for a heavy pseudoscalar boson A decaying to Zh, in the final states with $h \rightarrow \tau\tau$,” Phys. Lett. B **755**, 217-244 (2016).
- [68] ATLAS Collaboration, “Search for pair production of Higgs bosons in the $b\bar{b}b\bar{b}$ final state using proton–proton collisions at $\sqrt{s} = 13$ TeV with the ATLAS detector,” ATLAS-CONF-2016-049.
- [69] CMS Collaboration, “Search for a massive resonance decaying to a pair of Higgs bosons in the four b quark final state in proton-proton collisions at $\sqrt{s} = 13$ TeV,” arXiv:1710.04960.
- [70] CMS Collaboration, “Search for Higgs boson pair production in events with two bottom quarks and two tau leptons in proton-proton collisions at $\sqrt{s} = 13$ TeV,” arXiv:1707.02909.
- [71] CMS Collaboration, “Combination of searches for Higgs boson pair production in proton-proton collisions at $\sqrt{s} = 13$ TeV,” Phys. Rev. Lett. **122**, 121803 (2019).
- [72] CMS Collaboration, “Search for resonant pair production of Higgs bosons in the $bbZZ$ channel in proton-proton collisions at $\sqrt{s} = 13$ TeV,” arXiv:2006.06391.
- [73] ATLAS Collaboration, “Reconstruction and identification of boosted di- τ systems in a search for Higgs boson pairs using 13 TeV proton–proton collision data in ATLAS,” arXiv:2007.14811.

- [74] CMS Collaboration, V. Khachatryan *et al.*, “Search for a pseudoscalar boson decaying into a Z boson and the 125 GeV Higgs boson in $\ell^+\ell^-b\bar{b}$ final states,” *Phys. Lett. B* **748**, 221-243 (2015).
- [75] ATLAS Collaboration, G. Aad *et al.*, “Search for a CP-odd Higgs boson decaying to Zh in pp collisions at $\sqrt{s} = 8$ TeV with the ATLAS detector,” *Phys. Lett. B* **744**, 163-183 (2015).
- [76] ATLAS Collaboration, “Search for heavy resonances decaying into a W or Z boson and a Higgs boson in final states with leptons and b-jets in 36 fb^{-1} of $\sqrt{s} = 13$ pp collisions with the ATLAS detector,” arXiv:1712.06518.
- [77] CMS Collaboration, “Search for a heavy pseudoscalar boson decaying to a Z and a Higgs boson at $\sqrt{s} = 13$ TeV,” *Eur. Phys. Jour. C* **79**, 564 (2019).
- [78] CMS Collaboration, “Search for a heavy pseudoscalar Higgs boson decaying into a 125 GeV Higgs boson and a Z boson in final states with two tau and two light leptons at $\sqrt{s} = 13$ TeV,” arXiv:1910.11634.
- [79] ATLAS Collaboration, “Search for Higgs bosons decaying to aa in the $\mu\mu\tau\tau$ final state in pp collisions at $\sqrt{s} = 8$ TeV with the ATLAS experiment,” *Phys. Rev. D* **92**, 052002 (2015).
- [80] CMS Collaboration, “Search for light bosons in decays of the 125 GeV Higgs boson in proton-proton collisions at $\sqrt{s} = 8$ TeV,” *JHEP* **1710**, 076 (2017).
- [81] CMS Collaboration, “Search for an exotic decay of the Higgs boson to a pair of light pseudoscalars in the final state with two b quarks and two τ leptons in proton-proton collisions at $\sqrt{s} = 13$ TeV,” *Phys. Lett. B* **785**, 462 (2018).
- [82] CMS Collaboration, “Search for light pseudoscalar boson pairs produced from decays of the 125 GeV Higgs boson in final states with two muons and two nearby tracks in pp collisions at $\sqrt{s} = 13$ TeV,” arXiv:1907.07235.
- [83] CMS Collaboration, “Search for a light pseudoscalar Higgs boson in the boosted $\mu\mu\tau\tau$ final state in proton-proton collisions at $\sqrt{s} = 13$ TeV,” arXiv:2005.08694.
- [84] CMS Collaboration, V. Khachatryan *et al.*, “Search for neutral resonances decaying into a Z boson and a pair of b jets or τ leptons,” *Phys. Lett. B* **759**, 369-394 (2016).
- [85] ATLAS Collaboration, “Search for a heavy Higgs boson decaying into a Z boson and another heavy Higgs boson in the $\ell\ell b\bar{b}$ final state in p p collisions $\sqrt{s} = 13$ TeV with the ATLAS detector,” *Phys. Lett. B* **783**, 392 (2018).
- [86] CMS Collaboration, “Search for new neutral Higgs bosons through the $H \rightarrow ZA \rightarrow \ell^+\ell^-b\bar{b}$

- process in pp collisions at $\sqrt{s}=13$ TeV,” arXiv:1911.03781.
- [87] A. Alloul et al., *Comput. Phys. Commun.* **185**, 2250 (2014).
 - [88] G. Belanger, F. Boudjema, A. Pukhov, A. Semenov, *Comput. Phys. Commun.* **185**, 960-985 (2014).
 - [89] G. Jungman, M. Kamionkowski, K. Griest, *Phys. Rept.* **267**, 195 (1996); M. A. Shifman, A. I. Vainshtein, V. I. Zakharov, *Phys. Lett. B* **78**, 443 (1978).
 - [90] Planck Collaboration, *Astron. Astrophys. A* **27**, 594 (2016).
 - [91] E. Aprile et al. [XENON Collaboration], *Phys. Rev. Lett.* **121**, 111302 (2018).
 - [92] Fermi-LAT Collaboration, *Phys. Rev. Lett.* **115**, 231301 (2015).
 - [93] S. R. Coleman and E. J. Weinberg, *Phys. Rev. D* **7**, 1888 (1973).
 - [94] L. Dolan and R. Jackiw, *Symmetry Behavior at Finite Temperature*, *Phys. Rev. D* **9**, 3320–3341 (1974).
 - [95] M. E. Carrington, *Phys. Rev. D* **45**, 2933–2944 (1992).
 - [96] P. B. Arnold and O. Espinosa, *Phys. Rev. D* **47**, 3546 (1993) [Erratum: *Phys. Rev. D* **50**, 6662 (1994)].
 - [97] I. Affleck, *Phys. Rev. Lett.* **46**, 388 (1981).
 - [98] A. D. Linde, *Nucl. Phys. B* **216**, 421 (1983) [Erratum: *Nucl. Phys. B* **223**, 544 (1983)].
 - [99] A. D. Linde, *Phys. Lett. B* **100**, 37-40 (1981).
 - [100] C. L. Wainwright, *Comput. Phys. Commun.* **183**, 2006–2013 (2012).
 - [101] P. Athron, C. Balázs, A. Fowlie and Y. Zhang, *Eur. Phys. J. C* **80**, no.6, 567 (2020) doi:10.1140/epjc/s10052-020-8035-2 [arXiv:2003.02859 [hep-ph]].
 - [102] D. Bodeker and G. D. Moore, *JCAP* **0905**, 009 (2009).
 - [103] D. Bodeker and G. D. Moore, *JCAP* **1705**, 025 (2017).
 - [104] D. Bodeker and G. D. Moore, *JCAP* **1705**, 025 (2017).
 - [105] M. Hindmarsh, S. J. Huber, K. Rummukainen, and D. J. Weir, *Phys. Rev. D* **92**, 123009 (2015).
 - [106] J. Kozaczuk, *JHEP* 1510, 135 (2015).
 - [107] J. M. No, *Phys. Rev. D* **84**, 124025 (2011).
 - [108] M. Maziashvili, *JCAP* **1006**, 028 (2010).
 - [109] A. Kosowsky, A. Mack and T. Kahniashvili, *Phys. Rev. D* **66**, 024030 (2002).
 - [110] C. Caprini, R. Durrer and G. Servant, *JCAP* **0912**, 024 (2009).

- [111] P. Binetruy, A. Bohe, C. Caprini and J.-F. Dufaux, JCAP **1206**, 027 (2012).
- [112] P. Athron et al., arXiv:1901.03714.